RAA 2019 Vol. **19** No. **8**, 114(12pp) doi: 10.1088/1674–4527/19/8/114

http://www.raa-journal.org *http://iopscience.iop.org/raa*

Research in Astronomy and Astrophysics

AstroSat observation of GX 5–1: spectral and timing evolution

Yashpal Bhulla[1], Ranjeev Misra[2], J. S. Yadav[3] and S. N. A Jaaffrey[1]

[1] Pacific Academy of Higher Education and Research University, Udaipur-313003, India; *yash.pkn@gmail.com*
[2] Inter-University Center for Astronomy and Astrophysics, Pune-411007, India
[3] Tata Institute of Fundamental Research, Mumbai-400005, India

Received 2018 November 4; accepted 2019 February 17

Abstract We report on the first analysis of an *AstroSat* observation of the Z-source GX 5–1 on 2017 February 26−27. The hardness-intensity plot reveals that the source traced out the horizontal and normal branches. The 0.8−20 keV spectra from simultaneous SXT and LAXPC data at different locations of the hardness-intensity plot can be described well by disk emission and a thermal Comptonized component. The ratio of the disk flux to the total flux, i.e., the disk flux ratio, increases monotonically along the horizontal branch to the normal one. Thus, the difference between the normal and horizontal branches is that in the normal branch, the disk dominates the flux while in the horizontal one it is the Comptonized component which dominates. The disk flux scales with the inner disk temperature as $T_{\rm in}^{5.5}$ and not as $T_{\rm in}^{4}$, suggesting that either the inner radius changes dramatically or that the disk is irradiated by the thermal component changing its hardness factor. The power spectra reveal a quasi-periodic oscillation (QPO) whose frequency changes from ∼30 Hz to 50 Hz. The frequency is found to correlate well with the disk flux ratio. In the 3−20 keV LAXPC band, the r.m.s. of the QPO increases with energy (r.m.s. $\propto E^{0.8}$), while the harder X-rays seem to lag the soft ones with a time-delay of milliseconds. The results suggest that the spectral properties of the source are characterized by the disk flux ratio and that the QPO has its origin in the corona producing the thermal Comptonized component.

Key words: accretion — accretion disc — stars: neutron star — X-rays: binaries — X-rays: individual: GX 5–1

1 INTRODUCTION

X-ray binaries are a class of binaries that emit X-ray radiation. An X-ray binary system has a normal star or a white dwarf transferring mass onto a compact object such as a neutron star (NS) or a black hole (BH). These systems can be classified into two categories, i.e., low-mass X-ray binaries (LMXBs) and high-mass X-ray binaries (HMXBs), based on the mass of the companion star (Hasinger & van der Klis 1989). In LMXBs, the low mass companion star is usually a late type star and matter accretes through Roche lobe overflow (e.g., Konar & Bhattacharya 1999; Paul & Naik 2011).

LMXBs harboring NSs can be characterized into two classes called "Atoll" and "Z" based on the shapes they trace out in their X-ray hardness intensity diagram (HID) (e.g., Atoll-type: 4U 1608–52 (Lei et al. 2015); GX 3+1 (Kuulkers & van der Klis 2000); 4U 1735–44 (Lei et al. 2013); 4U 1728–34 (Migliari et al. 2003); 4U 1820–30 (Díaz Trigo et al. 2017); GX 9+1 (Wang 2016) and Z-type: Cyg X-2 (Lei et al. 2013); GX 17+2 (Kuulkers et al. 2002); GX 349+2 (Iaria et al. 2004); Sco X-1 (Titarchuk et al. 2001); GX 340+0 (Seifina et al. 2013); GX 5–1 (Jackson et al. 2009); (Hasinger & van der Klis 1989)). The HID is a plot of hardness as a function of total X-ray count rates. HID plot representations are useful for understanding the variations in spectra and spectral components.

The Z-type sources are characterized by having three main branches in an HID. From top-left to bottom-right is the horizontal branch (HB), and then the normal branch (NB) and the bottom flaring branch (FB). The transition between the NB and HB is called the hard apex (HA) and that between the FB and NB is called the soft apex (Blom et al. 1993; Agrawal & Bhattacharyya 2003). Z-type sources are further subdivided into two subcategories: those with a somewhat vertical or short HB, but with an extended long FB, are called "Sco like sources," e.g., Sco X-1, GX 17+2 and GX 349+2, while those sources that have a proper horizontal HB and weak FB are called "Cyg like

sources," e.g., Cyg X-2, GX 340+0 and GX 5–1 (Penninx et al. 1991; Kuulkers et al. 1994; Church et al. 2012).

Theoretically, for NS-LMXBs the X-ray emission may originate from the accretion disk and a boundary layer between the disk and the NS's surface (Hanawa 1989; Popham & Sunyaev 2001; Gilfanov et al. 2003). Observationally, the spectra of these sources are dominated by a Comptonized component and a soft one. There has been controversy regarding the origin of these components. In one interpretation, the soft component is due to a multi-colored disk and the Comptonized one is due to the boundary layer (Mitsuda et al. 1984; Makishima et al. 1986; Mitsuda et al. 1989; Barret et al. 1999; Agrawal & Misra 2009) while the alternative is that the soft component is blackbody emission from the boundary layer and the Comptonized one is due to a corona (Church & Bałucińska-Church 2004; Kong et al. 2006; Lavagetto et al. 2008). In fact, some spectral analyses suggest the more natural situation that the seed photons arise from two components (i.e., blackbody and disk emission) or that one can dominate at different regions of the Z-track (Raichur et al. 2011; Sakurai et al. 2012; Armas Padilla et al. 2017). The spectral parameters vary along the track but are subject to which interpretation is chosen (Falanga et al. 2006; White et al. 1988; Titarchuk et al. 1998; Agrawal & Sreekumar 2003). It has been argued that changes in the mass accretion rate, $\dot{M}$, are responsible for a source changing its spectral state or moving along its branches in the HID, as proposed by Priedhorsky et al. (1986). Support for an increase of $\dot{M}$ from the HB to the NB, and then along the FB, came from a multi-wavelength study of Cyg X-2 by Hasinger et al. (1990). In the past decade, however, it has been shown that the variability of Z sources is not as simple as this (Church et al. 2012). For example, spectral analysis along the Z-track suggests that the accretion rate may be constant (Lin et al. 2009).

Another debate in the literature has been the location and size of the region producing the Comptonizing component. For eclipsing sources, the time taken for the companion star to eclipse the X-ray producing region suggests a large size of $\sim 10^{11}$ cm (Church & Bałucińska-Church 2004) and hence the spectra of these sources have been interpreted in terms of the extended accretion disk corona model (Church et al. 2014). An extended hot region is also required to produce the ionized emission lines seen in high resolution spectra (Schulz et al. 2009). However it is not clear how the gravitational energy that is released close to the NS is transported to power such an extended corona. More importantly, as discussed below, these sources exhibit high frequency quasi-periodic oscillations (QPOs) which demand a highly compact origin of the Comptonized component instead of an extended one.

Timing studies are an important possible way to constrain the geometry and interpret the changes along the Z-track. These studies are generally undertaken by computing the power spectral density (PSD) which is the amplitude squared of the Fourier transform of the source light curve. It generally consists of broad features along with narrow peaks with the latter being called QPOs (Méndez & van der Klis 1999; van der Klis 2000; Méndez 2000; Méndez et al. 2001; Barret et al. 2005; Mondal et al. 2018). It should be noted that most of these studies are based on analysis of data from the *Rossi X-ray Timing Explorer* (*RXTE*). QPOs have been observed in the horizontal and normal branches which are named horizontal branch oscillations (HBOs) and normal branch oscillations (NBOs) respectively (van der Klis et al. 1985; Lamb 1991; Lewin et al. 1992). The frequencies of the HBOs lie in the range $15-60$ Hz while for NBOs they lie between $5-20$ Hz (Jonker et al. 2002; Homan et al. 2007). It is also known that the frequencies evolve along the track, i.e. the HBO frequency decreases from the HA as the source moves along the HB and the frequency is correlated with intensity. These sources also show very rapid variability in the form of kHz QPOs which are seen when the source is in the normal and flaring branches (Kuulkers et al. 1996; Wijnands et al. 1998).

GX 5–1 is the second brightest (after Sco X-1, (Giacconi et al. 1962)) persistent NS LMXB. The source is classified as a Z-track LMXB and is located near the Galactic center. It radiates nearly at or exceeding the Eddington limit with typical Eddington fraction $L/L_{\rm edd} = 1.6-2.3$ assuming a distance of 9.0 kpc (Jackson et al. 2009; Sriram et al. 2011; Homan et al. 2018). It is a Cyg-like source having an extended HB (Kuulkers et al. 1994). The source exhibits NBO and HBO along with kHz QPOs (Wijnands & van der Klis 1999; Jonker et al. 2002). The frequency of its HBO ranges from 13 to 50 Hz and is known to correlate with X-ray luminosity (van der Klis et al. 1985). Hard time lags (i.e., the hard photons are delayed with respect to the soft ones) of the order of milliseconds have been detected for both HBOs and NBOs (van der Klis et al. 1987; Vaughan et al. 1994; Sriram et al. 2011).

RXTE spectral analysis of GX 5–1 was conducted by Jackson et al. (2009), who favored a blackbody with Comptonized components (which they refer to as an extended accretion disk corona model) over one where the emission is from a multi-color disk and Comptonization. However, Sriram et al. (2011) found by analyzing *RXTE* data that the multi-color disk and Comptonization component provided an acceptable fit and identified evidence for variation in the inner disk radius. They also showed the root mean square (r.m.s.) of the QPOs observed in both

the normal and horizontal branches increases with energy, suggesting an origin in the inner regions. A more extensive work involving a larger number of *RXTE* observations confirmed these basic results (Sriram et al. 2012). However, we note that such analyses were hampered by the absence of data below 3 keV. *Nuclear Spectroscopic Telescope Array* (*NuSTAR*) observation (again limited to energies above 3 keV) of GX 5–1 also showed a blackbody component with temperature ∼2.5 keV at the HB, which was interpreted as a boundary layer component (Homan et al. 2018).

AstroSat is the first Indian Multi-wavelength satellite. The Large Area X-ray Proportional Counter (LAXPC) consists of three identical proportional counter units (PCUs) having a total effective area of $\sim$6000 cm^2 at 15 keV and provides event data lists which can be used effectively to compute the PSD for different energy bands (Yadav et al. 2016a; Agrawal et al. 2017; Antia et al. 2017). The LAXPC is well complimented by the Soft X-ray Telescope (SXT) allowing simultaneous coverage in the soft energy band (Singh et al. 2017). The LAXPC has already enabled unprecedented data to study the rapid temporal behavior of BH systems (Yadav et al. 2016b; Misra et al. 2017; Bhargava et al. 2017; Pahari et al. 2018). It has detected kHz QPOs and burst oscillation from the NS system 4U 1728-34 (Verdhan Chauhan et al. 2017) and has revealed detailed information on the source's thermonuclear bursts (Bhattacharyya et al. 2018). Spectral and timing properties of the Atoll-source 4U 1705-44 along the banana track have been characterized by LAXPC (Agrawal et al. 2018). One of the primary advantages of studying NS systems such as GX 5–1 by *AstroSat* is the simultaneous broad band spectral data (0.7−30 keV provided by LAXPC and SXT) with high resolution timing data. This provides a unique opportunity to study the connection between temporal (long and short term) properties of the source and its spectral components.

In this work, we present results of *AstroSat* data analysis targeting the Z-source GX 5–1. To the best of our knowledge, this is the first time that both LAXPC and SXT data have been used to track an NS source as it evolves in its hardness diagram. The timing information from LAXPC is combined with wide band spectra of the LAXPC/SXT to model the spectral and temporal evolution of this source.

2 OBSERVATIONS AND DATA ANALYSIS

GX 5–1 was observed by *AstroSat* from 2017 February 26 17:34:56 to 2017 February 27 06:45:17 for an effective exposure time of ∼35 ks. The LAXPC data were analyzed using LAXPC software (`http://astrosat-ssc.iucaa.in/?q=laxpcData`) to obtain background subtracted light curves, photon spectra, PSDs and frequency dependent time lags. To take into account LAXPC response uncertainties, a systematic error of 3% was used for spectral fitting. The LAXPC spectra were fitted from 3−20 keV since the data were background dominated at higher energies. The SXT spectra and light curves were extracted using XSELECT (XSELECT V2.4d) from level-2 data. A circular region with a 12′ radius was used for source extraction. Due to uncertainties in the effective area and response, the SXT spectra were considered in the energy range 0.8−6 keV and a gain fit correction was included. Simultaneous spectral fittings for both the instruments were carried out using XSPEC version 12.9.1.

Figure 1 displays the LAXPC and SXT background light curves binned to 2.3778 s, i.e., at the SXT time resolution. The LAXPC light curve is the sum of all three detectors and is for the energy range 3−20 keV while for SXT it is 0.8−6 keV. Data gaps are due to South Atlantic Anomaly (SAA) passages, Earth occultation and instrument shutdowns. SXT operations are at nighttime and hence its efficiency in viewing is less than that of LAXPC. The vertical lines mark the common time for the two instruments and, as described in the next section, spectral analysis has been done for strict simultaneous data.

We define hardness as the ratio between the LAXPC count rate in the 8−20 keV range divided by that in 3−8 keV. The hardness was computed for 60 second time bins and is plotted against the total count rate (or intensity) in the 3−20 keV band in Figure 2. In such an HID, portions of the Z-track are clearly distinguished. The source shows an extended HB, an HA and an NB. No FB is seen for this observation. The NB corresponds to the start of the observation when in a timescale of a few ks the source traced out the entire branch. For most of the observation, the source was in the HA and HB.

For spectral and timing analysis, we partitioned the Z-track into six distinct regions. The HB was divided into three regions named HB-1, HB-2 and HB-3. The HA region was named HA and the NB was split into two: the lower normal branch (LNB) and upper normal branch (UNB). The selected regions for the horizontal and normal branches are shown as rectangular boxes in Figure 2. The remaining part of the HID was marked as HA. The regions have been chosen to roughly span the Z-track and the effective exposure times for simultaneous LAXPC and SXT data of the LNB, UNB, HA, HB-1,HB-2 and HB-3 are 1080, 2140, 3557, 490, 484 and 304 s respectively.

3 SPECTRAL ANALYSIS AND RESULTS

Spectral fitting was undertaken for each of the six different locations along the Z-track. For each location, only that time-segment which was strictly simultaneous with an

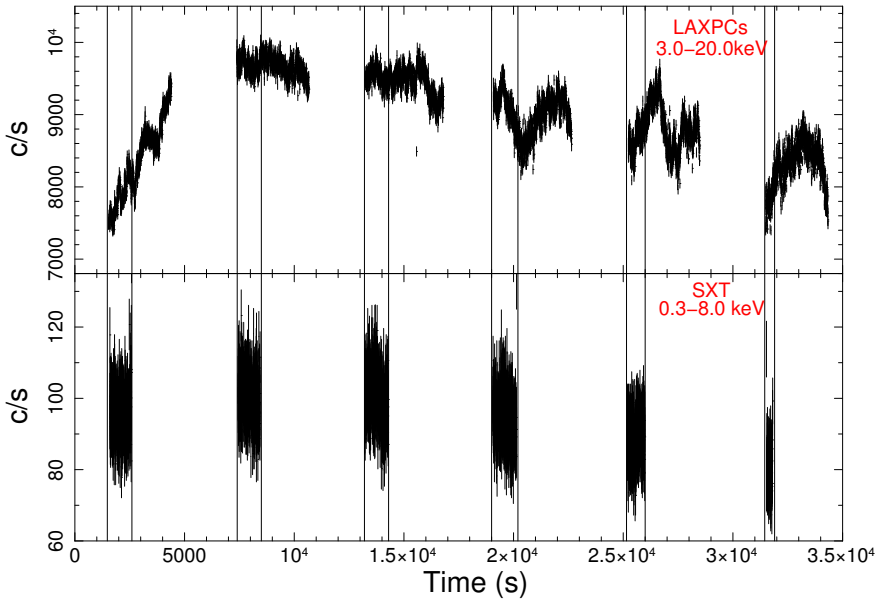

Fig. 1 Background subtracted light curve of GX 5–1. The time bin is 2.3778 s at the SXT time resolution. The *vertical lines* mark the regions from which strict simultaneous spectra were obtained.

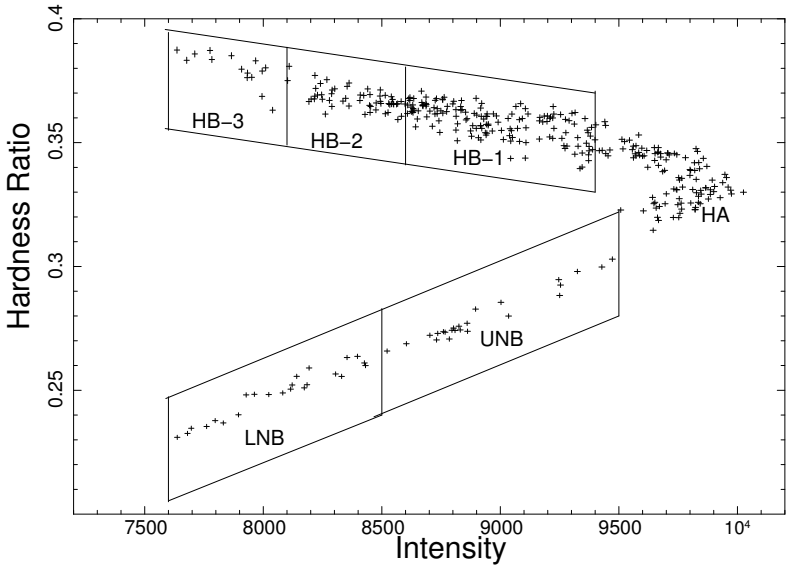

Fig. 2 HID of GX 5–1 observed with *AstroSat*/LAXPC. The horizontal and normal branches are clearly seen, which are subdivided into six regions for spectral analysis.

SXT observation was taken into consideration. This is illustrated in Figure 1, where the vertical lines mark the time for which spectra were analyzed. The exception was for the UNB where there is no corresponding SXT observation and thus for this segment, only the LAXPC data were considered.

We first fitted a two component model consisting of a Comptonized component and a blackbody one represented by the XSPEC routine "nthcomp" and "bbodyrad" respectively. The absorption was taken into account by the XSPEC routine "tbabs." The blackbody was assumed to be the seed photon source of the Comptonizing medium, i.e. the temperature of the blackbody was tied to the input seed photon temperature during fitting and the shape of the seed photon was taken to be blackbody. While the fit produced reasonable χ^2, the normalization of the blackbody component was extremely high. Since the normalization of the routine "bbodyrad" represents the radius of the blackbody sphere ($N_{\rm bbodyrad} = R^2_{\rm km}/D^2_{10\ \rm kpc}$), we found that for a distance of $D = 9$ kpc, the radius turned out to have an un-

Table 1 Best-fit parameter values of the individual location of LAXPCS spectra as well as the combined burst spectrum with SXT data.

Location	$N_{\rm H}$	$N_{\rm dbb}$	$R_{\rm in}$	$kT_{\rm in}$	Γ	$kT_{\rm e}$	$F_{\rm T}$	$F_{\rm D}/F_{\rm T}$	χ^2_ν/dof
LNB	$2.75^{+0.04}_{-0.04}$	$226^{+25.32}_{-20.22}$	$19.13^{+1.04}_{-0.88}$	$1.40^{+0.17}_{-0.12}$	$2.52^{+0.09}_{-0.13}$	$2.92^{+1.60}_{-0.60}$	$4.13^{+0.02}_{-0.03}$	$0.40^{+0.01}_{-0.01}$	1.35/523
**UNB	2.75^{f}	185^{f}	17.31	$1.44^{+0.05}_{-0.06}$	$2.68^{+0.06}_{-0.07}$	$3.94^{+0.21}_{-0.17}$	$3.41^{+0.03}_{-0.04}$	$0.34^{+0.01}_{-0.02}$	0.82/24
HA	$2.74^{+0.02}_{-0.01}$	$177^{+11.10}_{-10.41}$	$16.93^{+0.52}_{-0.51}$	$1.46^{+0.04}_{-0.05}$	$2.10^{+0.07}_{-0.08}$	$2.88^{+0.05}_{-0.04}$	$4.70^{+0.02}_{-0.02}$	$0.32^{+0.01}_{-0.01}$	1.67/546
HB1	$2.73^{+0.03}_{-0.03}$	$183^{+36.073}_{-39.48}$	$17.20^{+1.63}_{-2.01}$	$1.30^{+0.16}_{-0.14}$	$2.08^{+0.05}_{-0.05}$	$2.85^{+0.20}_{-0.27}$	$4.26^{+0.04}_{-0.03}$	$0.23^{+0.01}_{-0.01}$	1.15/547
HB2	$2.67^{+0.06}_{-0.02}$	$119^{+42.18}_{-45.71}$	$13.88^{+2.26}_{-2.93}$	$1.26^{+0.09}_{-0.15}$	$2.06^{+0.05}_{-0.06}$	$2.97^{+0.23}_{-0.16}$	$4.15^{+0.05}_{-0.03}$	$0.13^{+0.01}_{-0.01}$	1.13/523
HB3	$2.69^{+0.10}_{-0.08}$	$98^{+13.81}_{-16.45}$	$12.60^{+0.85}_{-1.15}$	$0.96^{+0.09}_{-0.09}$	$2.05^{+0.03}_{-0.04}$	$2.95^{+0.05}_{-0.05}$	$3.84^{+0.08}_{-0.06}$	$0.03^{+0.06}_{-0.01}$	1.07/428

$N_{\rm H}$ is absorption column density in units of $\times\ 10^{22}$ atom cm^2. $N_{\rm dbb} = \{R_{\rm in}/D_{10}\}^2 \times \cos i$ is the normalization of the disk blackbody component. $R_{\rm in}$ is inner disk radius in km computed from $N_{\rm dbb}$ assuming a distance of 9 kpc and inclination angle of 60°. $kT_{\rm in}$ is the inner disk temperature. Γ and $kT_{\rm e}$ are the photon index and electron temperature of the thermal Comptonization component. $kT_{\rm in}$ and $kT_{\rm e}$ are in the unit of keV. $F_{\rm T}$ and $F_{\rm D}$ are the unabsorbed bolometric flux and the flux of the disk component with unit erg cm^{-2} s^{-1}. (^{f}) denotes that the parameter was frozen, (**) indicates that at this location there was no SXT observation and hence spectral fitting is done with LAXPC data alone.

physically large value of ∼2000 km or more. This is true for all the segments considered with SXT data.

Our favored model is the one where the blackbody is replaced by a multi-color disk blackbody (XSPEC routine: "diskbb") and the form of the seed photon for the Comptonization is taken to be such disk emission. The best fit parameters for the model are tabulated in Table 1 and a typical unfolded spectrum with residuals is shown in Figure 3. The parameters are the normalization of the disk component $N_{\rm dbb}$, the inner disk temperature $kT_{\rm in}$, the temperature of the Comptonizing medium $kT_{\rm e}$ and the photon index Γ of the Comptonized component. The disk normalization is related to inner disk radius (in km) $R_{\rm km}$ by $= (R_{\rm km}/D_{10\,\rm kpc})^2 \times \cos i$, where $D_{10\,\rm kpc}$ is the distance to the source in units of 10 kpc and i is the inclination angle of the disk. The best fit values of the normalization are ∼180, indicating reasonable values for the inner disk radius of ∼20 km. Note that the disk normalization and absorption column density could not be constrained for the UNB due to the absence of SXT data and for that spectrum the normalization and column density were fixed. Hence the UNB has been excluded from further analysis.

We note that there have been several works where more complex models have been invoked to fit the spectra from such sources (e.g., Homan et al. 2018; Lin et al. 2009). In general, these models have three components instead of the two employed here and hence we tested the possibility of including another component. Specifically, we added an additional blackbody emission component in the model consisting of disk emission and thermal Comptonization. We find that for all the spectra considered the decrease in χ^2 is less than 3 and hence the data do not justify the inclusion of a third component. We have also tried other variations of the three component model, such as assuming that the seed photon for the thermal component is due to the blackbody instead of the disk, but again find no significant improvement in the fitting. We note that despite having a broader energy coverage than *RXTE*, we are unable to justify the use of more complex three component models as employed by Lin et al. (2009). We suspect that the 3% systematic error that is included for the LAXPC and SXT spectra does not allow for a more complex model to be constrained and we discuss the implications of this in the last section.

The unabsorbed bolometric fluxes (in the $0.001 - 100$ keV range) were computed using the XSPEC function "cflux" for the total and for the disk component. The total flux and the ratio of the disk flux to the total (which we call the disk flux ratio) are tabulated in Table 1. While the total flux varies non-uniformly, the disk flux ratio has remarkablely monotonic behavior, increasing along the HB and NB in a uniform manner. This is illustrated more clearly in the left panel of Figure 4, where the hardness ratio (8−20 keV by 3−8 keV) of the segment is plotted against the disk flux ratio. Thus, the location of the source in the horizontal and normal branches is determined by the value of the disk flux ratio, making it the single parameter determining the spectral state of the system. We also note that the disk flux itself is found to be proportional to the disk flux ratio as shown in the right panel of Figure 4. The disk flux itself may be the main driver behind the variability, a point which is discussed in the last section. There is no significant qualitative variation in the Comptonization parameters, namely the electron temperature, $kT_{\rm e}$, and photon index, Γ.

The inner disk radius shows variability, which is more clearly exhibited by plotting the inner disk temperature versus the disk flux as displayed in Figure 5. For a constant inner radius, the flux should scale as $T_{\rm in}^4$, but instead the flux scales more steeply as $T_{\rm in}^{5.5}$. It may also be possible

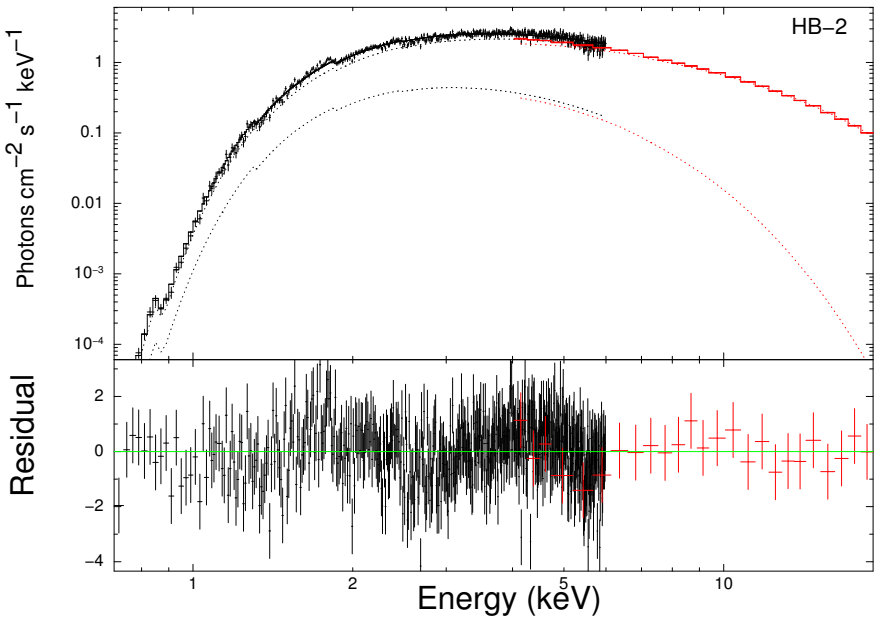

Fig. 3 The unfolded spectrum 0.8−6 keV SXT (*black*) and 3−20 keV LAXPC (*red*) in the spectrum of GX 5–1 for the HB2 region.

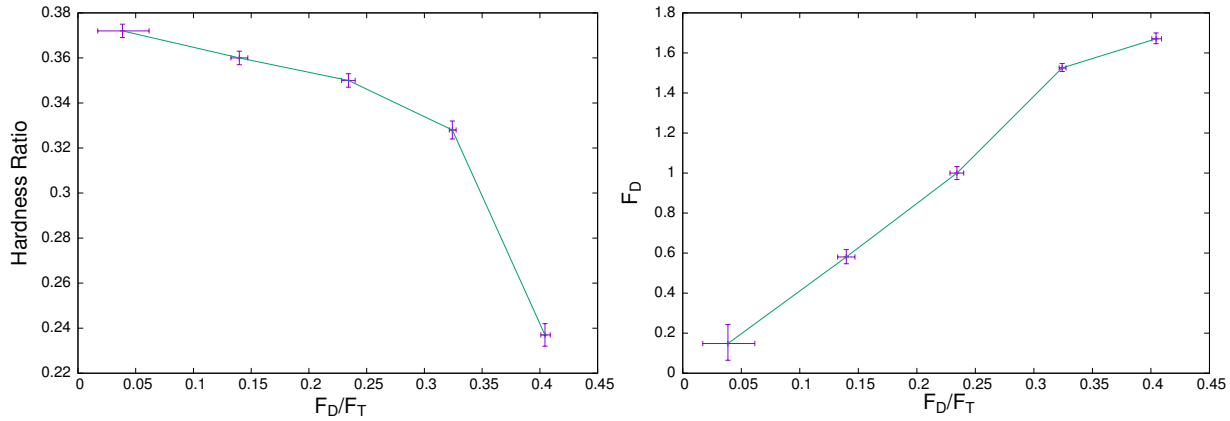

Fig. 4 *Left Panel*: Plot of hardness ratio as defined in Fig. 2 versus the disk flux ratio $F_{\rm D}/F_{\rm T}$; *Right Panel*: Variation of the bolometric disk flux $F_{\rm D}$ with disk flux ratio $F_{\rm D}/F_{\rm T}$.

and perhaps more likely that the color factor of the disk is changing (perhaps due to irradiation) causing this steeper variation, while the inner disk radius is more or less constant. On the other hand, this may also indicate that the model used here is simple and a more complex spectral model may be needed.

4 TIMING ANALYSIS

PSDs were computed for each of the Z-track sections in the 3−20 keV band. All three LAXPC counters were used in the timing analysis and the expected dead time corrected Poisson noise level was subtracted from each power spectrum which was normalized such that the integration of the power spectra gave the fractional r.m.s. variation. The top panels of Figure 6 show the power spectra for the three sections of the HB. A clear QPO is detected which dominates the power spectra. The power spectra were fitted using three Lorentzians corresponding to the QPO, its harmonic and a zero centered low frequency broad band noise for the HB sections. For the HA and NB, the harmonic is not seen while another broad feature at ∼5 Hz is required by the data. The best fit values of the fitting are tabulated in Table 2. For the NB, the QPO was not detected in the two individual sections, due to the shorter exposure time and hence we combined the two sections into one and the power spectrum is shown in the bottom right panel of Figure 6. We note that the low frequency component has significantly increased in the NB. The QPO frequency in-

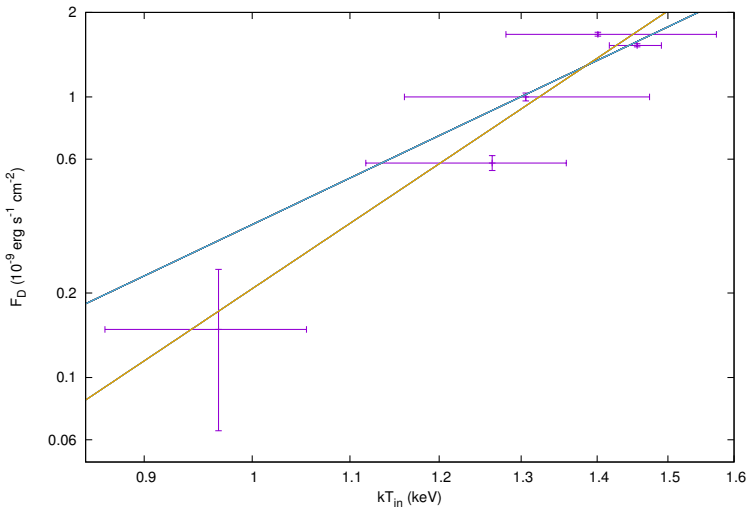

Fig. 5 Variation of the inner disk temperature $kT_{\rm in}$ with the disk flux $F_{\rm D}$. The best fit curve $F \propto T^{5.5}$ is marked in *yellow*. Also shown is the relation $F \propto T^4$ in *cyan*. The data seem to not be consistent with $F \propto T^4$, i.e., a constant inner disk radius.

Table 2 Best-fitting QPO Values from NB to HB-3

Location	$^*NB$	HA	HB-1	HB-2	HB-3
ν_1	0	0	0	0	0
σ_1	$2.53^{+0.52}_{-0.47}$	$3.47^{+0.57}_{-0.55}$	$18.64^{+1.35}_{-2.52}$	$13.30^{+1.33}_{-1.18}$	$10.08^{+1.32}_{-1.16}$
$N_1(\times10^{-4})$	$0.23^{+0.1}_{-0.1}$	$2.39^{+0.36}_{-0.37}$	$13.90^{+4.9}_{-4.1}$	$21.29^{+0.96}_{-0.97}$	$26.30^{+1.5}_{-1.5}$
ν_2	$5.99^{+0.70}_{-0.65}$	$5.35^{+1.28}_{-1.44}$	-	-	-
σ_2	$4.65^{+2.46}_{-1.76}$	$19.62^{+0.40}_{-0.38}$	-	-	-
$N_2(\times10^{-4})$	$2.28^{+0.67}_{-0.09}$	$5.38^{+0.36}_{-0.43}$	-	-	-
ν_3	$49.62^{+0.48}_{-0.57}$	$39.53^{+0.18}_{-0.16}$	$37.22^{+0.17}_{-0.17}$	$34.20^{+0.16}_{-0.17}$	$30.19^{+0.09}_{-0.10}$
σ_3	$6.97^{+2.37}_{-1.79}$	$19.36^{+0.64}_{-1.1}$	$8.99^{+0.64}_{-0.59}$	$7.66^{+0.80}_{-0.70}$	$4.52^{+0.15}_{-0.15}$
$N_3(\times10^{-4})$	$0.81^{+0.57}_{-0.31}$	$6.85^{+0.14}_{-0.13}$	$7.97^{+0.28}_{-0.39}$	$12.07^{+0.77}_{-0.74}$	$13.67^{+1.1}_{-1.1}$
ν_4	-	-	$74.22^{+4.67}_{-5.82}$	$68.31^{+7.18}_{-7.08}$	$58.41^{+4.59}_{-5.11}$
σ_4	-	-	$15.39^{+2.57}_{-7.42}$	$15.32^{+4.68}_{-4.51}$	$18.04^{+1.96}_{-6.28}$
$N_4(\times10^{-4})$	-	-	$6.32^{+0.27}_{-0.27}$	$11.20^{+0.83}_{-0.79}$	$20.60^{+0.72}_{-0.71}$

ν_1, ν_2, ν_3 and ν_4 are the frequencies in Hz, σ_1, σ_2, σ_3 and σ_4 are the full widths at half maximum (FWHMs) in keV, and N_1, N_2, N_3 and N_4 are the normalizations of the Lorentzians. $(^*)$ indicates the QPO is for the full NB region, since it was not detected individually in the LNB or UNB due to poor statistics.

creases monotonically along the HB to the NB, where the frequency is plotted against disk flux ratio. However, its fractional r.m.s. decreases (right panel of Fig. 9).

The event mode data of LAXPC allow for computing the temporal properties in several energy bins. Power spectra were analyzed for different energy bins and the fractional r.m.s. obtained from fitting a Lorentzian to the QPO was estimated for the different energy bins.

Figure 7 shows the variation of the fractional r.m.s. with energy for the three sections of the HB and the HA. The statistics for the NB were not good enough to do such an analysis. The variation of r.m.s. with energy is similar for all the sections. It increases with energy and its functional dependence can be described as $\propto E^{0.8}$.

LAXPC data also facilitate computation of the time lag as a function of energy. To compute the time lag, the Fourier transforms were calculated with a frequency bin equal to the full width at half maximum (FWHM) of the QPO and lags were computed at the QPO frequency with respect to the reference energy band of 5−7 keV.

Figure 8 displays the time lag as a function of energy for the different sections of the HB and the HA. It seems that the HB segments show positive hard time lag (i.e. the high energy photons are delayed compared to the soft ones) while for the HA it is the opposite. The positive time lag

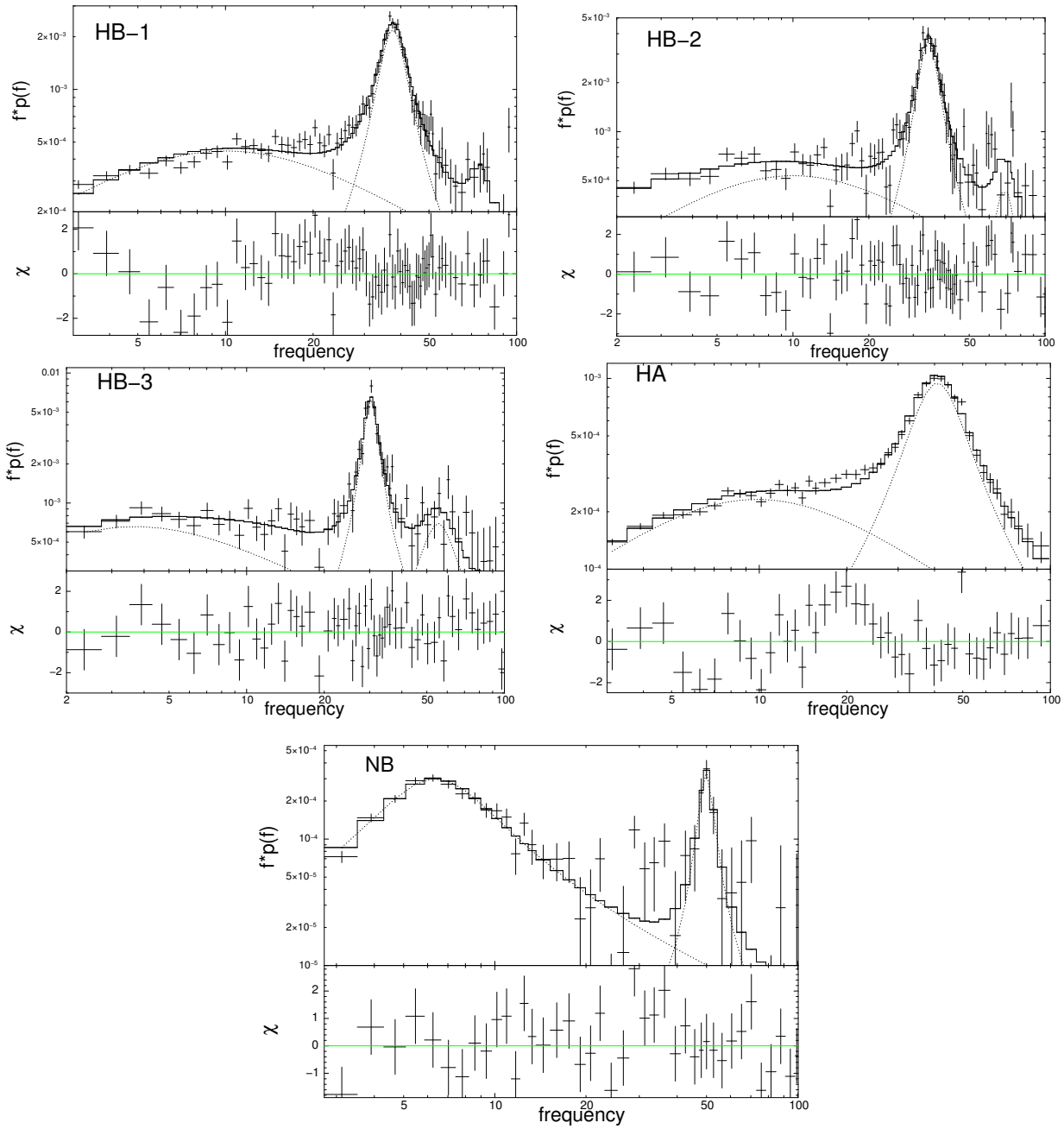

Fig. 6 *AstroSat* power spectra of GX 5–1 for each of the five locations of the Z-track in the energy range 3−20 keV. The power spectra have been fitted by three Lorentzian components, and the best fit parameters are listed in Table 2.

seen in the HB does not seem to be correlated with the position in the Z-track. However, since the statistics are not good this may not be significant and we caution against overinterpretation. What is clear is that the magnitude of the time lags is less than a few milliseconds.

5 SUMMARY AND DISCUSSION

We present the analysis of an *AstroSat* observation of the Z-track source GX 5–1. We used the strictly simultaneous SXT and LAXPC data to track the spectrum of an NS source as it moves along its HID and at the same time quantify the rapid temporal variability of the source. During the observation, GX 5–1 traced out the normal and horizontal branches in its HID which was divided into six segments and analyzed separately.

The primary results are:

• The broad band SXT/LAXPC spectra from 0.8−20 keV were fitted with an absorbed blackbody and thermal component, but the radius of the blackbody turned out to be unphysically large at ∼2000 km. On the other hand, an absorbed disk emission and a thermal Comptonized compo-

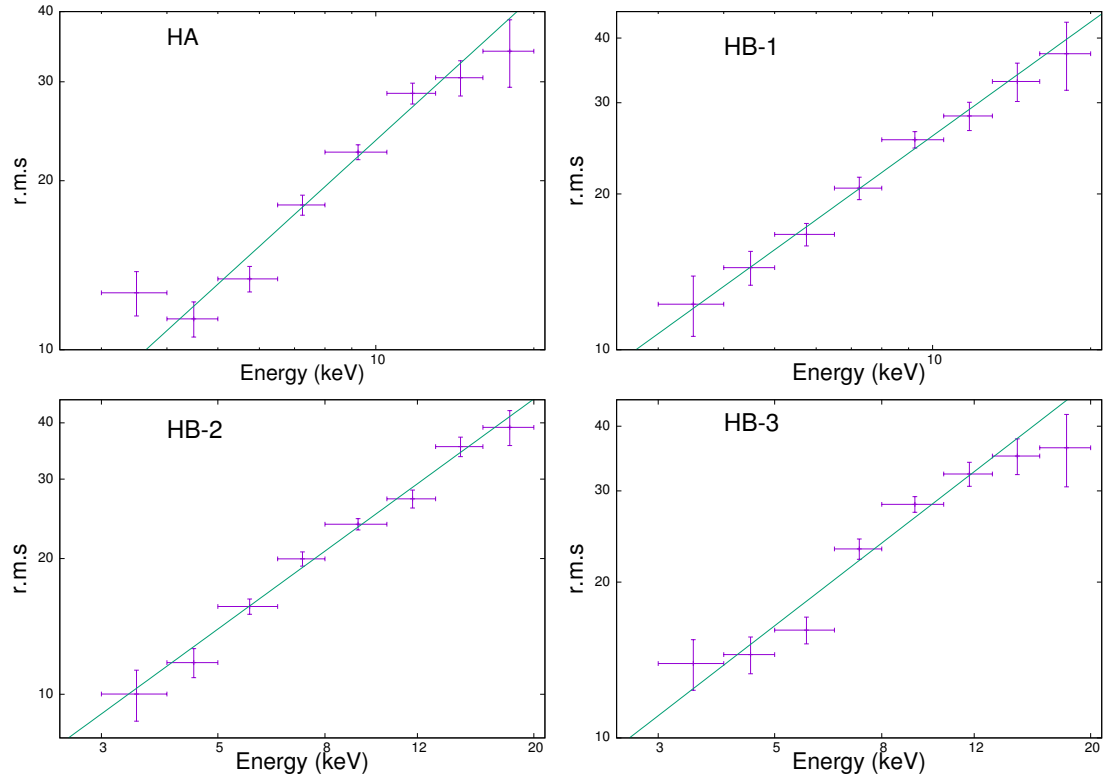

Fig. 7 The r.m.s. of the QPO versus photon energy for three different regions of the HB and the HA. The r.m.s. roughly increases with energy $\propto E^{0.8}$.

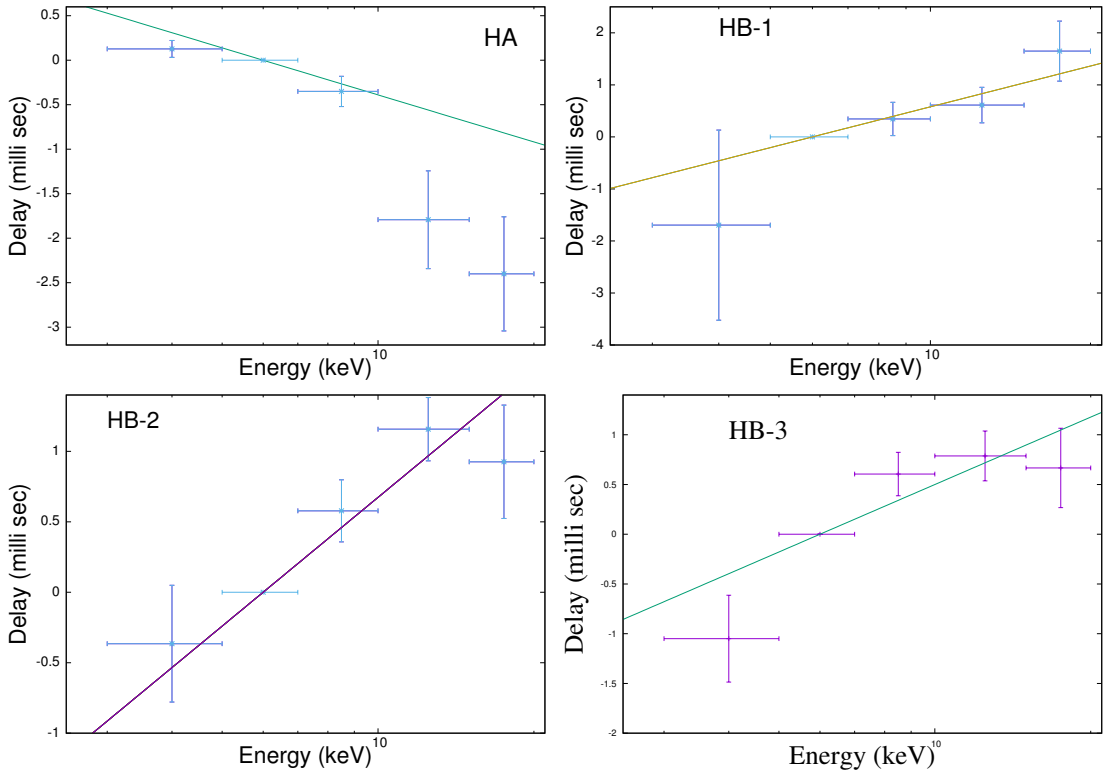

Fig. 8 Time lag at the QPO frequency with respect to the 5−7 keV band versus energy for three different regions of the HB and the HA. While the time lags seem to be hard for the HB, they seem to be soft for the HA. However, the statistics are not good. Note that the time lags are constrained to be less than a few milliseconds.

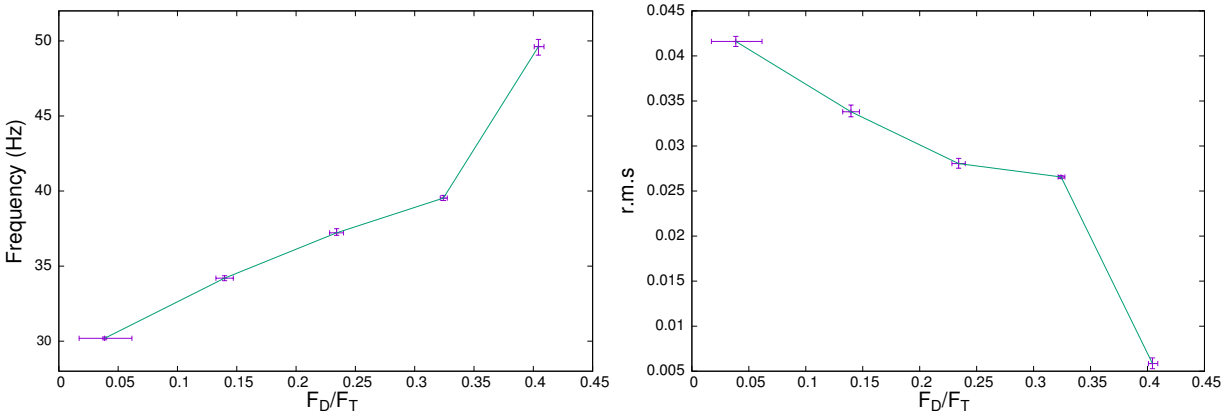

Fig. 9 The variation of the QPO frequency and r.m.s. as a function of the disk flux ratio $F_{\rm D}/F_{\rm T}$. While the frequency increases with the ratio, the r.m.s. decreases.

nent fitted the data well, and the inner disk radius turned out to be reasonable, i.e., ∼20 km. Thus the latter model was preferred.

• The disk flux ratio, defined as the ratio of the bolometric unabsorbed disk flux to the total unabsorbed flux, decreased monotonically along the HB to the normal one, indicating that this may be the primary driver which determines the location of the source in the Z diagram. However, we note that the disk flux itself is correlated with the disk flux ratio. The disk flux varies as $T_{\rm in}^{5.5}$, indicative of a varying inner radius or changes in the color factor.

• The power spectra for all sections of the Z-track show a QPO at ∼50 Hz. The QPO is dominant in the HB while its strength decreases in the normal one, where the power spectrum also has a pronounced low frequency component. The QPO frequency increases, while its r.m.s. decreases with disk flux ratio. The r.m.s. of the QPO increases with energy ($\propto E^{0.8}$) for all sections of the Z-track. The time lags between different energy bins are constrained to be less than a few milliseconds.

One of the important clues regarding the temporal behavior of these systems is to identify the physical parameter (or at least the spectral parameter) that determines the source's position in the HID diagram. Our results suggest that this may be related to the disk flux ratio. Thus the difference in hardness for horizontal and normal branches (at the same intensity level) is the contribution of the disk to the total flux. It is interesting to note that there is also a correlation between the disk flux and the disk flux ratio, perhaps indicating that the disk flux itself is the primary driver. If that is the case, and if we assume that the inner disk radius does not vary much, then the disk flux would be proportional to the accretion rate, and one could retrieve the physically attractive proposition that the accretion rate itself determines the state of the system. However, this implies that the total flux and, in particular, the flux of the thermal Comptonization component do not scale with accretion rate. For an NS system with a surface, one expects the total flux to be proportional to the accretion rate since, unlike a BH, the accretion efficiency cannot be small, due to advection. On the other hand, if a significant amount of energy or matter is expelled to a jet or wind, then the radiative flux may indeed not be proportional to the accretion rate. Such a speculation needs to be followed up with evidence for jet or wind activity, perhaps in non X-ray wavebands.

The spectral analysis undertaken in this work seems to imply that there are only two spectral components, namely the disk emission and a thermal component. This is in contrast to other works (e.g., Lin et al. 2009), where a third blackbody component has been included even though the energy band used in this work, 0.8−20 keV, is broader than that of the *RXTE* analysis >3 keV. Note that for spectral analysis of *RXTE* data, the column density was taken to be fixed, while here the presence of low energy data allows us to constrain it. It is not clear whether the broader energy band constrains the fitting to have a smaller number of components or if the systematic error used for the fitting (3%) is too large to discriminate between competing models. This may be the reason why in this analysis the disk flux does not scale as temperature to the fourth power, while the analysis of Lin et al. (2009) showed such a scaling for the three component model. Low energy spectral coverage from data from other instruments like NICER will be useful to determine whether the spectrum is a simple or complex one.

The rapid temporal behavior of the source shows a strong QPO at ∼50 Hz whose frequency increases, while its r.m.s. decreases with the disk flux ratio. Energy dependent analysis of the QPO reveals that the r.m.s. is an increasing function of energy and time lags between high and low energy photons are less than a few millisec-

onds. This implies that the QPO originates in the thermal Comptonized component and it weakens when the component is less dominant, as has been shown earlier using *RXTE* data (Sriram et al. 2011). Detailed radiative modeling of these energy dependent properties will shed light on the driver and the geometry of the system. The QPO frequency should be associated with some characteristic timescale of the system, which in turn may be related to come characteristic radius. Since the timescale should decrease with radius, the frequency should be inversely proportional to such a radius. It is tempting to associate this radius with that of the inner disk. While the inner disk radius estimated in the spectral fitting may be subjected to several uncertainties such as the spectral model used, color factor, etc, it is interesting to see the correlation between frequency and disk flux ratio. This is qualitatively expected if the disk flux ratio is inversely related to the inner disk radius.

The broad band spectral coverage provided by SXT/LAXPC along with the rapid timing capabilities of the LAXPC has provided a unique opportunity to study these NS systems. Note, for example, that when there was no simultaneous SXT spectrum for the upper section of the NB, the disk normalization and absorption column density were not constrained, which highlights the importance of SXT for such analysis. Indeed, other observations by *AstroSat* of GX 5–1 and other such sources will provide insight into their temporal behavior.

Acknowledgements We thank members of the LAXPC instrument team for their contribution to the development of the LAXPC instrument. We also acknowledge contributions of the *AstroSat* project team at ISAC. This paper makes use of data from the *AstroSat* mission of the Indian Space Research Organisation (ISRO), archived at the Indian Space Science Data Centre (ISSDC). We also acknowledge the support of LAXPC POC as well as SXT POC at TIFR.

References

Agrawal, P. C., Yadav, J. S., Antia, H. M., et al. 2017, Journal of Astrophysics and Astronomy, 38, 30
Agrawal, V. K., & Bhattacharyya, S. 2003, A&A, 398, 223
Agrawal, V. K., & Misra, R. 2009, MNRAS, 398, 1352
Agrawal, V. K., Nandi, A., Girish, V., & Ramadevi, M. C. 2018, MNRAS, 477, 5437
Agrawal, V. K., & Sreekumar, P. 2003, MNRAS, 346, 933
Antia, H. M., Yadav, J. S., Agrawal, P. C., et al. 2017, ApJS, 231, 10
Armas Padilla, M., Ueda, Y., Hori, T., Shidatsu, M., & Muñoz-Darias, T. 2017, MNRAS, 467, 290
Barret, D., Grindlay, J. E., Harrus, I. M., & Olive, J. F. 1999, A&A, 341, 789
Barret, D., Olive, J.-F., & Miller, M. C. 2005, MNRAS, 361, 855
Bhargava, Y., Rao, A. R., Singh, K. P., et al. 2017, ApJ, 849, 141
Bhattacharyya, S., Yadav, J. S., Sridhar, N., et al. 2018, ApJ, 860, 88
Blom, J. J., Int-Zand, J. J. M., Heise, J., et al. 1993, A&A, 277, 77
Church, M. J., & Bałucińska-Church, M. 2004, MNRAS, 348, 955
Church, M. J., Gibiec, A., & Bałucińska-Church, M. 2014, MNRAS, 438, 2784
Church, M. J., Gibiec, A., Bałucińska-Church, M., & Jackson, N. K. 2012, A&A, 546, A35
Díaz Trigo, M., Migliari, S., Miller-Jones, J. C. A., et al. 2017, A&A, 600, A8
Falanga, M., Goetz, D., Goldoni, P., et al. 2006, VizieR Online Data Catalog, 345
Giacconi, R., Gursky, H., Paolini, F. R., & Rossi, B. B. 1962, Physical Review Letters, 9, 439
Gilfanov, M., Revnivtsev, M., & Molkov, S. 2003, A&A, 410, 217
Hanawa, T. 1989, ApJ, 341, 948
Hasinger, G., & van der Klis, M. 1989, A&A, 225, 79
Homan, J., Steiner, J. F., Lin, D., et al. 2018, ApJ, 853, 157
Homan, J., van der Klis, M., Wijnands, R., et al. 2007, ApJ, 656, 420
Iaria, R., Di Salvo, T., Robba, N. R., et al. 2004, ApJ, 600, 358
Jackson, N. K., Church, M. J., & Bałucińska-Church, M. 2009, A&A, 494, 1059
Jonker, P. G., van der Klis, M., Homan, J., et al. 2002, MNRAS, 333, 665
Konar, S., & Bhattacharya, D. 1999, MNRAS, 308, 795
Kong, A. K. H., Charles, P. A., Homer, L., Kuulkers, E., & O'Donoghue, D. 2006, MNRAS, 368, 781
Kuulkers, E., Homan, J., van der Klis, M., Lewin, W. H. G., & Méndez, M. 2002, A&A, 382, 947
Kuulkers, E., & van der Klis, M. 2000, in Rossi2000: Astrophysics with the Rossi X-ray Timing Explorer, ed. T. E. Strohmayer, 72
Kuulkers, E., van der Klis, M., Oosterbroek, T., et al. 1994, A&A, 289, 795
Kuulkers, E., van der Klis, M., & Vaughan, B. A. 1996, A&A, 311, 197
Lamb, D. Q. 1991, PASP, 103, 760
Lavagetto, G., Iaria, R., D'Ai, A., di Salvo, T., & Robba, N. R. 2008, ChJAA (Chin. J. Astron. Astrophys.), 8S, 325
Lei, Y.-J., Zhang, H.-T., Zhang, C.-M., et al. 2013, AJ, 146, 60
Lei, Y., Zhang, H., & zhang, Y. 2015, IAU General Assembly, 22, 2257059
Lewin, W. H. G., Lubin, L. M., Tan, J., et al. 1992, MNRAS, 256, 545
Lin, D., Remillard, R. A., & Homan, J. 2009, in American

Astronomical Society Meeting Abstracts, 213, 603.03
Makishima, K., Maejima, Y., Mitsuda, K., et al. 1986, ApJ, 308, 635
Méndez, M. 2000, Nuclear Physics B Proceedings Supplements, 80, 15
Méndez, M., & van der Klis, M. 1999, ApJ, 517, L51
Méndez, M., van der Klis, M., & Ford, E. C. 2001, ApJ, 561, 1016
Migliari, S., Fender, R. P., Rupen, M., et al. 2003, MNRAS, 342, L67
Misra, R., Yadav, J. S., Verdhan Chauhan, J., et al. 2017, ApJ, 835, 195
Mitsuda, K., Inoue, H., Nakamura, N., & Tanaka, Y. 1989, PASJ, 41, 97
Mitsuda, K., Inoue, H., Koyama, K., et al. 1984, PASJ, 36, 741
Mondal, A. S., Dewangan, G. C., Pahari, M., & Raychaudhuri, B. 2018, MNRAS, 474, 2064
Pahari, M., Yadav, J. S., Verdhan Chauhan, J., et al. 2018, ApJ, 853, L11
Paul, B., & Naik, S. 2011, Bulletin of the Astronomical Society of India, 39, 429
Penninx, W., Lewin, W. H. G., Tan, J., et al. 1991, MNRAS, 249, 113
Popham, R., & Sunyaev, R. 2001, X-ray Astronomy: Stellar Endpoints, AGN, and the Diffuse X-ray Background, 599, 870
Priedhorsky, W., Hasinger, G., Lewin, W. H. G., et al. 1986, ApJ, 306, L91
Raichur, H., Misra, R., & Dewangan, G. 2011, MNRAS, 416, 637
Sakurai, S., Yamada, S., Torii, S., et al. 2012, PASJ, 64, 72
Schulz, N. S., Huenemoerder, D. P., Ji, L., et al. 2009, ApJ, 692, L80
Seifina, E., Titarchuk, L., & Frontera, F. 2013, ApJ, 766, 63
Singh, K. P., Stewart, G. C., Westergaard, N. J., et al. 2017, Journal of Astrophysics and Astronomy, 38, 29
Sriram, K., Choi, C. S., & Rao, A. R. 2012, ApJS, 200, 16
Sriram, K., Rao, A. R., & Choi, C. S. 2011, ApJ, 743, L31
Titarchuk, L. G., Bradshaw, C. F., Geldzahler, B. J., & Fomalont, E. B. 2001, ApJ, 555, L45
Titarchuk, L., Lapidus, I., & Muslimov, A. 1998, ApJ, 499, 315
van der Klis, M. 2000, ARA&A, 38, 717
van der Klis, M., Hasinger, G., Stella, L., et al. 1987, ApJ, 319, L13
van der Klis, M., Jansen, F., van Paradijs, J., et al. 1985, IAU Circ., 4140
Vaughan, B., van der Klis, M., Lewin, W. H. G., et al. 1994, ApJ, 421, 738
Verdhan Chauhan, J., Yadav, J. S., Misra, R., et al. 2017, ApJ, 841, 41
Wang, J. 2016, International Journal of Astronomy and Astrophysics, 6, 82
White, N. E., Stella, L., & Parmar, A. N. 1988, ApJ, 324, 363
Wijnands, R., Méndez, M., van der Klis, M., et al. 1998, ApJ, 504, L35
Wijnands, R., & van der Klis, M. 1999, ApJ, 514, 939
Yadav, J. S., Misra, R., Verdhan Chauhan, J., et al. 2016a, ApJ, 833, 27
Yadav, J. S., Agrawal, P. C., Antia, H. M., et al. 2016b, in Proc. SPIE, 9905, Space Telescopes and Instrumentation 2016: Ultraviolet to Gamma Ray, 99051D